ACSNANO
www.acsnano.org
ARTICLE

Size-Selective Nanoparticle Assembly on Substrates by DNA Density Patterning

Benjamin D. Myers,[†,‡] Qing-Yuan Lin,[†] Huanxin Wu,[§] Erik Luijten,[†,§,∥] Chad A. Mirkin,[†,⊥,#] and Vinayak P. Dravid*[,†,‡,⊥]

[†]Department of Materials Science and Engineering, Northwestern University, Evanston, Illinois 60208, United States
[‡]NUANCE Center, Northwestern University, Evanston, Illinois 60208, United States
[§]Department of Physics and Astronomy, Northwestern University, Evanston, Illinois 60208, United States
[∥]Department of Engineering Sciences and Applied Mathematics, Northwestern University, Evanston, Illinois 60208, United States
[⊥]International Institute for Nanotechnology, Northwestern University, Evanston, Illinois 60208, United States
[#]Department of Chemistry, Northwestern University, Evanston, Illinois 60208, United States

Supporting Information

ABSTRACT: **The vision of nanoscale self-assembly research is the programmable synthesis of macroscale structures with controlled long and short-range order that exhibit a desired set of properties and functionality. However, strategies to reliably isolate and manipulate the nanoscale building blocks based on their size, shape, or chemistry are still in their infancy. Among the promising candidates, DNA-mediated self-assembly has enabled the programmable assembly of nanoparticles into complex architectures. In particular, two-dimensional assembly on substrates has potential for the development of integrated functional devices and analytical systems. Here, we combine the high-resolution patterning capabilities afforded by electron-beam lithography with the DNA-mediated assembly process to enable direct-write grayscale DNA density patterning. This method allows modulation of the functionally active DNA surface density to control the thermodynamics of interactions between nanoparticles and the substrate. We demonstrate that size-selective directed assembly of nanoparticle films from solutions containing a bimodal distribution of particles can be realized by exploiting the cooperativity of DNA binding in this system. To support this result, we study the temperature-dependence of nanoparticle assembly, analyze the DNA damage by X-ray photoelectron spectroscopy and fluorescence microscopy, and employ molecular dynamics simulations to explore the size-selection behavior.**

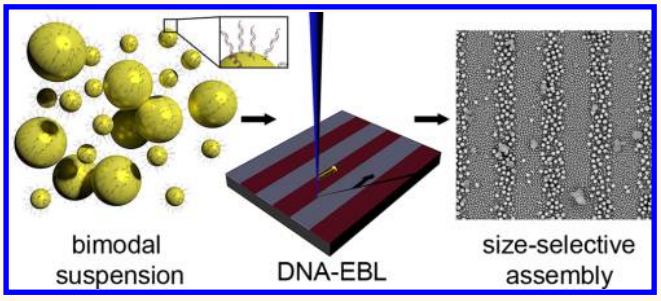

KEYWORDS: *DNA nanotechnology, self-assembly, directed assembly, electron-beam lithography, nanopatterning, nanoparticle assembly*

The assembly of nanoparticles into larger ensembles with well-controlled architecture[1−3] has enabled the development of new materials for potential application in plasmonics,[4−6] sensing,[7,8] photovoltaics,[9] and data storage.[10] Among the various assembly strategies,[11−13] DNA-mediated nanoparticle assembly has emerged as a powerful and versatile approach due to the highly specific, tunable, and reversible nature of DNA binding.[2,3,14] DNA-programmable self-assembly has resulted in the development of a range of interesting structures from clusters to three-dimensional (3D) colloidal crystals with control over lattice parameter, symmetry, and crystal habit.[15−17] Specific macroscopic crystal structures based on nanoparticle motifs can be synthesized by following a well-defined set of design rules and tuning parameters such as nanoparticle size and DNA length.[16] Two-dimensional (2D) DNA-mediated nanoparticle assembly on surfaces[18,19] has been applied in microarray technology,[8,20] and recently, interest has emerged in this technique for the fabrication of structures with novel optical properties.[21−23] Many of the critical parameters in 3D assembly have been identified, notably the effect of DNA density on the melting (particle-dissociation) temperature of colloidal crystals,[24−26] but its role in 2D assembly has not been studied and exploited systematically.

Electron-beam lithography (EBL) has matured as a flexible nanopatterning tool,[27,28] and electron irradiation has been shown to cause damage to DNA and individual nucleo-

Received: April 2, 2016
Accepted: May 18, 2016
Published: May 18, 2016

DOI: 10.1021/acsnano.6b02246
ACS Nano 2016, 10, 5679−5686

bases.[29,30] Therefore, one could envision that selectively damaging a DNA monolayer by electron-beam patterning would give rise to controlled particle−substrate interactions. Whereas electron-beam patterning of self-assembled monolayers has been shown previously,[31,32] this study demonstrates the use of DNA-EBL to tune the density of functionally active DNA in a monolayer by grayscale (*i.e.*, nonbinary) DNA patterning. The effectiveness of this technique for DNA density patterning is confirmed by X-ray photoelectron spectroscopy (XPS) and fluorescence microscopy. DNA-EBL enables patterning of DNA density with high spatial resolution for multiplexed analysis of 2D nanoparticle assembly. This approach differs from yet complements previous studies on 3D assembly which require multiple batches of nanoparticles with different DNA densities and analysis by indirect methods of spectrophotometry[33] or fluorimetry.[34] In this work, we build on the design rules in the complementary contact model (CCM)[16] and extend the understanding to particle−surface interactions. Specifically, DNA density patterning by DNA-EBL drives the size-selective assembly of nanoparticles from a solution with a bimodal distribution of particles. We show that for nanoparticles with the same surface chemistry, the size distribution of particles can be controlled such that smaller particles preferentially associate with areas of high DNA density and larger particles assemble in lower density regions. We substantiate the former observation with a thermodynamic argument based on geometric surface coverage akin to the CCM and show that the transition from small to large particles with decreasing DNA density occurs due to particle-size effects and collective binding at the individual particle level, as supported by molecular dynamics (MD) simulations.

RESULTS AND DISCUSSION

The assembly method in this study relies on four oligonucleotides, which include two anchor strands and two linker strands, as used in previous work.[2,35] The DNA anchor strands are attached to the gold nanoparticles (A-anchor) and the gold-coated silicon surface (B-anchor), and subsequently, the A- and B-linker strands are hybridized with the particle and surface-bound anchor strands, respectively. The anchor strands have an A_{10} spacer and an 18-base sequence complementary to the respective linker strand. The linker strands present five-base complementary "sticky ends" which enable the assembly of nanoparticles on the substrate. The key innovation in this work (Figure 1) is the use of DNA-EBL to modify the B-anchor DNA monolayer, which modulates the subsequent hybridization with B-linker DNA, effectively modulating the surface density of functionally active DNA. An EBL system is used to pattern arbitrary features with nanometer-scale resolution and precise electron-dose control over a wide range (20−10 000 $\mu C/cm^2$). This results in a high degree of control over the surface density of active DNA on the substrate and thereby enables tunable thermodynamic interactions during the subsequent nanoparticle-assembly process. Size-selective assembly is achieved due to strong size-dependent effects which drive small particles to areas of high DNA density and large particles to regions with lower density of active DNA. We explore the influence of electron dose, temperature, and relative nanoparticle concentration on the size-selective assembly process.

To correlate the electron-beam irradiation with changes in the specific binding of nanoparticles, X-ray photoelectron spectroscopy analysis was used to probe the mechanism of

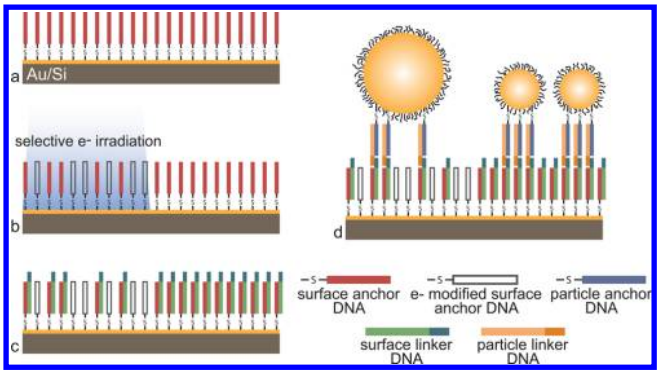

Figure 1. Schematic illustration of size-selective assembly process. (a) Thiol coupling of surface anchor DNA to Au-coated Si substrate. (b) DNA-EBL for dose-controlled electron-beam patterning of surface anchor DNA. (c) Hybridization of surface linker strands, showing reduced coverage in electron-irradiated regions. (d) Assembly of nanoparticles with different sizes but with the same surface functionalization. Larger particles are selectively adsorbed to regions that present a lower density of sticky ends.

damage to the DNA monolayers and fluorescence microscopy was used to probe the effect of this damage on the ability of the damaged anchor DNA to hybridize with linker strands. High-resolution XPS scans of the C 1s peak were captured for DNA monolayers as a function of increasing electron dose. The C 1s scan was fitted by four peaks, which correspond well to the characteristic peaks for DNA oligomers previously identified.[36] Similar to previous XPS studies on radiation damage of DNA,[37] a significant increase in hydrocarbon bonding (C $1s_A$) accompanied by a decrease in the peak associated with carbon bound to nitrogen (C $1s_B$) was found with increasing electron dose (Figure 2a). This change in carbon bonding indicates a cross-linking mechanism, which is consistent with previous studies that suggest this as the dominant damage mechanism for dry DNA irradiated in the absence of oxygen.[30] With increasing electron dose, an exponential decay in the C $1s_B$/C $1s_A$ peak area ratio was noted (Figure 2b).

However, whereas the XPS data show aggregate damage to the DNA monolayer, XPS does not directly probe the ability of the DNA to hybridize with linker strands. This is a critical difference as even a single base damaged by the electron beam could have a significant impact on nanoparticle binding.[8] To study the functional activity of the DNA after electron-beam modification, B-anchor DNA-functionalized substrates were patterned by DNA-EBL with a range of doses. Fluorescently labeled (Cy5) B-linker DNA strands were subsequently immobilized on the modified substrates. These substrates were then imaged by reflected-light fluorescence microscopy (Figure 2c), and comparison of the relative intensities of the modified regions to unmodified regions also showed exponential decay with electron dose (Figure 2d). A significant decrease in fluorescence intensity was seen with an electron dose as low as 20 $\mu C/cm^2$, which corresponds to approximately 22 incident electrons per DNA strand (assuming a DNA density of 9.6 pmol/cm^2).[38] While XPS results clearly indicate a cross-linking damage mechanism, further experiments are needed to determine the possible contribution and extent of other damage mechanisms such as individual base damage or desorption of the anchor DNA. However, these two studies clearly show that electron exposure leads to chemical changes in the anchor DNA that decrease the density of hybridized linker strands. Further, this change in DNA density is tunable

DOI: 10.1021/acsnano.6b02246
ACS Nano 2016, 10, 5679−5686

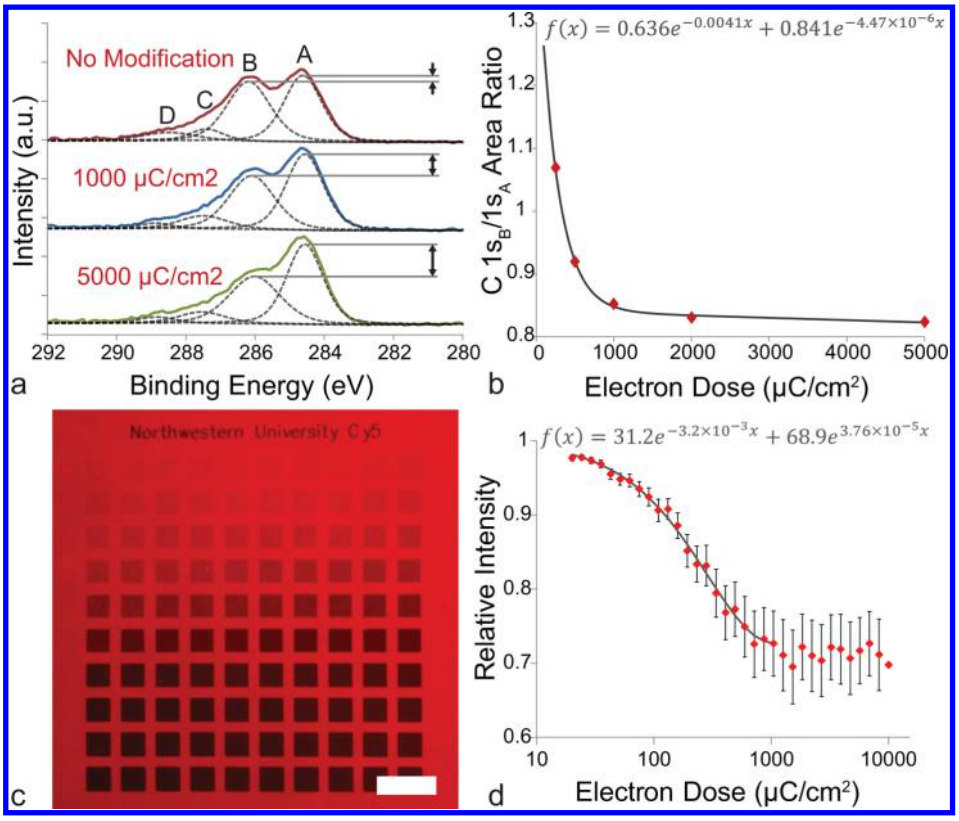

Figure 2. Verification and characterization of electron-beam modification of DNA. (a) High resolution XPS C 1s scans for an unmodified DNA monolayer compared to DNA exposed with doses of 1000 and 5000 μC/cm^2 showing significant change in the ratio of the C 1s$_A$ and 1s$_B$ peaks. (b) XPS data showing an exponential decay in the fitted peak-area ratio for C 1s$_B$/C 1s$_A$. (c) Fluorescence microscope image showing lithographically defined regions patterned by DNA-EBL with dose increasing exponentially from 20 μC/cm^2 (top-left) to 104 μC/cm^2 (bottom-right). (Scale bar is 100 μm.) (d) Change in relative fluorescence intensity as a function of electron dose indicating an exponential decay in active DNA density. Deviations from exponential behavior are likely due to fluorescence quenching at low doses (high DNA density) and limited sensitivity at high doses (low DNA density).

over a very wide range with a high degree of precision and high spatial resolution.

The ability to tune the DNA surface density in this manner is in itself a powerful tool with many potential applications. Here, we illustrate its use by controlling the adsorption from solutions with both unimodal and bimodal distributions of spherical DNA-modified gold nanoparticles in 0.5 M NaCl, 0.01 M sodium phosphate buffer (pH = 7.4). For monodisperse suspensions, this results in the ability to control the surface density of adsorbed particles (Figure 3a), which enables the site-specific tuning of nanoparticle monolayer density and the creation of surfaces with nanoparticle surface-density gradients. For solutions with a bimodal distribution of particles, we observe a complex competitive adsorption process in which the combined effects of particle size, DNA density, and temperature-dependent adsorption make it possible to control the relative surface density of particles based on their size (Figure 3b,c). This technique enables both binary size separation of particle mixtures on a surface and tuning of the size distribution for mixed monolayer nanoparticle films. In addition to the larger micrometer-scale features, the EBL system affords the ability to pattern features with length scales that are relevant to the study of photonic and plasmonic interactions and even down to the scale of individual particles. To demonstrate this capability, we created line patterns with controlled periodicity (Figure 3c) and linear arrays of 1D nanoparticle chains (Figure 3d,e). In these nanoparticle chains, the line width and pitch of the exposed lines not only arranged the particles in chains, but also allowed control of the size distribution of particles in the chain.

To study the impact of DNA density on the competitive adsorption of nanoparticles of different sizes in detail, we first investigated nanoparticle adsorption on DNA monolayers with no electron-beam modification. Nanoparticles were assembled at different temperatures on unmodified DNA-functionalized substrates from a solution with a bimodal distribution of small (30 nm) and large (80 nm) particles. The concentration of this mixed suspension was controlled to achieve small-to-large ratio of particles of approximately 42:1, with a total particle concentration of 2.56 nM. The results of these experiments showed nearly complete exclusion of the larger particles on the surface with a small-to-large ratio of 2.05×10^4:1 at 30 °C. As the assembly temperature was increased, this ratio decreased to 1.09×10^4:1 at 35 °C and 2.89×10^3:1 at 40 °C, and the overall density of the nanoparticle monolayers decreased by about 16% from 30 to 40 °C. This trend correlates with the size-dependent melting in these nanoparticle films as measured by spectrophotometry, which shows melting points of 48.9 °C for 30 nm particles and 53.1 °C for 80 nm particles. Melting curves are shown in Figure S1 of the Supporting Information. The difference in melting points has been exploited in previous work for particle−particle binding, enabling size separation of particles by sedimentation.[39] Similar effects were seen with lower small-to-large particle ratios as well (10:1 and 5:1),

DOI: 10.1021/acsnano.6b02246
ACS Nano 2016, 10, 5679−5686

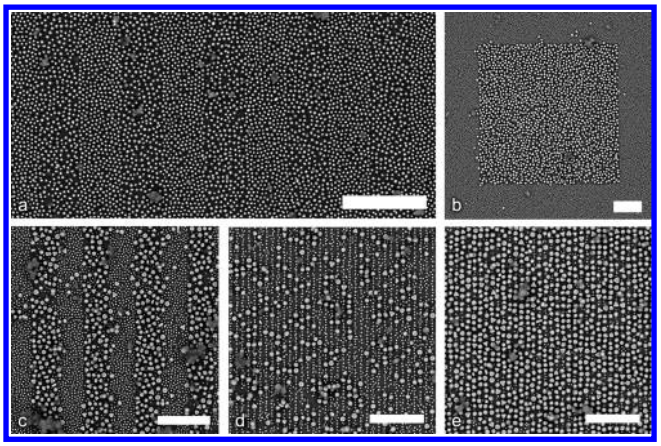

Figure 3. DNA-density directed assembly of small (30 nm) and large (80 nm) nanoparticles. (a) Shown are 500 nm line patterns with an electron dose of 470 μC/cm^2 to locally manipulate nanoparticle density for monodisperse particles (assembled at 35 °C). (b) Size-selective assembly from a solution with a bimodal distribution of particles (small-to-large particle ratio of 42:1) by exposing a 5 μm square with an electron dose of 990 μC/cm^2 (assembled at 35 °C). (c) Size-selective assembly with 500 nm line patterns with an electron dose of 510 μC/cm^2 (assembled at 40 °C). (d and e) High-resolution line patterning for 1D particle chains with control over particle size distribution. These patterns were created on the same substrate by exposing lines with a pitch of 110 nm and varying the line width ((d) 60 nm line width and 730 μC/cm^2; (e) 80 nm line width and 710 μC/cm^2; both assembled at 40 °C). (All scale bars are 1 μm.)

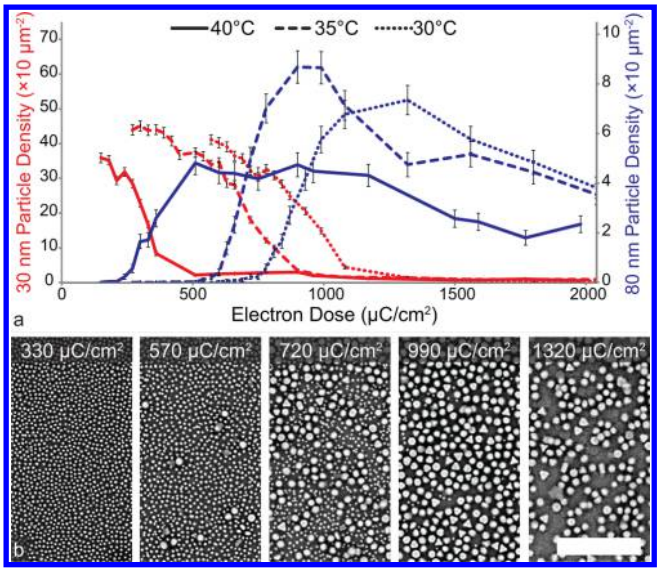

Figure 4. Temperature dependence of size-selective assembly. (a) Areal density of small and large particles as a function of electron dose showing a decrease in transition dose D_T (defined in the main text) with increasing assembly temperature. (*Y*-axis scales are adjusted to account for particle size and show equivalent surface coverage.) (b) Selected images of nanoparticle films showing electron-dose effects on small-to-large particle ratio for assembly at 35 °C. (Scale bar is 1 μm.)

indicating that this effect is driven primarily by particle−surface interactions (see Figure S2 in the Supporting Information) rather than concentration imbalance.

The combined effects of temperature- and size-dependent adsorption show a clear and tunable response when coupled with the precise control over local active DNA surface density afforded by DNA-EBL. A 15 keV electron beam was used to expose a series of 5-μm wide square regions with doses ranging from 150 to 2040 μC/cm^2 in 30 μC/cm^2 steps. The number density of particles was calculated as a function of electron dose at 30, 35, and 40 °C *via* image analysis (see Figure S4 in the Supporting Information). These data show a size-selective adsorption effect with a transition electron dose (D_T, defined as the dose resulting in equal areal coverage of small and large particles) that is temperature-dependent (Figure 4a). At low electron doses, the small particles dominate as in the unmodified films. As the dose is increased, the surface density of small particles decreases while the density of large particles increases, until the films are almost completely devoid of small particles. At higher doses, the density of the large particles also begins to decrease. A similar overall behavior is observed at all three assembly temperatures, but D_T shifts to lower doses as the temperature is increased.

This phenomenon enables the tuning of nanoparticle film size distribution from a situation dominated by small particles to one with predominantly large particles in one step and on the same substrate, starting from a mixed suspension (Figure 4b). These data show that the sensitivity of the adsorption and desorption rates to particle size can be varied dramatically by tuning the DNA density on the surface. With this method, ratios of 30 to 80 nm particles greater than 1:100 are achieved from a 42:1 ratio in the nanoparticle suspension, even without any optimization of the DNA sequences or immobilization chemistry. The actual discrimination is likely much higher as there are a significant number of agglomerated small particles that appear to behave as larger particles, but are still classified as small particles in the image analysis. It should be noted that effective size segregation requires nanoparticles densely functionalized with anchor strands and hybridized linker strands and a low concentration of free linker oligonucleotides in solution (see Figure S3 in the Supporting Information).

The size-selective assembly process demonstrated herein results from a competition between two phenomena that are both driven by the nanoparticle geometry. For unmodified DNA monolayers, the extremely high concentration of small particles in the nanoparticle film compared to the solution can be explained by their larger net surface interaction. A geometric analysis (see Figure S5 in the Supporting Information) shows that a close-packed, small-particle film has a 1.8-fold larger surface coverage than a large-particle film. Since the number of hybridized DNA strands is directly proportional to the contact area, this results in a significant enthalpic driving force similar to that described in the CCM.[16] As the DNA density is decreased by electron-beam modification, we hypothesize that the polyvalent nature of the DNA−nanoparticle binding is the primary driving force for the observed size-selective assembly. The probability that a particle encounters a sufficient number of linkages to immobilize it decreases with decreasing DNA density of the substrate and is dependent on nanoparticle size, resulting in a size-dependent variation of the adsorption rate and a corresponding shift in the equilibrium size distribution of the nanoparticle film. Similar effects have been shown in the assembly of 3D aggregates, where a minimum number of linkages between particles is required, leading to particle-size-dependent melting properties.[25]

To verify this hypothesis, we performed coarse-grained molecular dynamics simulations (Figure 5a and Videos 1 and 2 in the Supporting Information) and examined the effects of

DOI: 10.1021/acsnano.6b02246
ACS Nano 2016, 10, 5679−5686

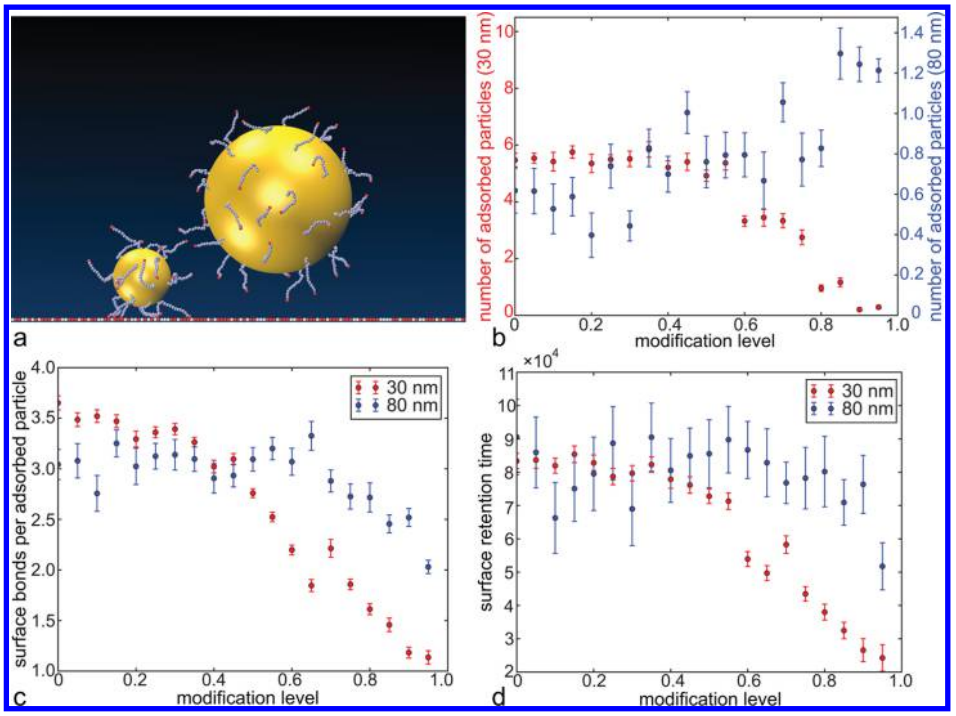

Figure 5. Molecular dynamics simulation of size-selective assembly. (a) Schematic illustration of simulated particles and substrate. (b) Size dependence of nanoparticle adsorption with decreasing DNA surface density (axes adjusted for equivalent projected area). (c) Average number of bonds involved in nanoparticle immobilization and (d) retention time for adsorbed particles for small and large particles.

Table 1. DNA sequences used in this study and their function

DNA function	DNA sequence (5′ to 3′)
A Anchor (NP)	TCA ACT ATT CCT ACC TAC AAA AAA AAA A SH
A Linker (NP)	GTA GGT AGG AAT AGT TGA ATC TCT
B Anchor (Substrate)	TCC ACT CAT ACT CAG CAA AAA AAA AAA A SH
B Linker (Substrate)	TTG CTG AGT ATG AGT GGA AAG AGA

particle size and DNA surface density on equilibrium nanoparticle adsorption. We modeled a bimodal distribution of nanoparticles matching the experimental setup, grafted with semiflexible bead−spring chains (each 14 beads long) that are capable of reversible attachment to surface binding sites. The solvent was modeled implicitly, with a Langevin thermostat for temperature control, whereas the modification of the DNA surface density was mimicked through variation of the density of binding sites. To account for the slow diffusion of the extended nanoparticles, we monitored their surface coverage for long times. We observed size-dependent adsorption as a function of DNA surface density (Figure 5b), with the smaller species dominating at low surface modification, but then monotonically decreasing and gradually being displaced by the larger species as the number of adsorption sites decreases, in agreement with the experimental observations. The coverage by the larger species grows steadily until curtailed by the sheer lack of binding sites. Accordingly, this mechanism could be exploited to segregate mixtures that contain additional species of different sizes or possibly binding strengths. The computational modeling also provides information that is less easily accessible experimentally. At the highest coverage by the smaller species, adsorbed nanoparticles were bound to the surface by more than three bonds (Figure 5c). This number dropped gradually with increasing modification level, preceding the decrease in nanoparticle coverage. As the larger species gradually replaced the smaller ones, their number of bonds per particle also surpassed the smaller species, reflecting stronger binding to the surface. Notably, for modification levels between 60% and 80%, the number of bonds continued to drop, whereas the coverage of the species increased. The surface residence time decreases more quickly with decreasing DNA surface density for small particles than for large particles (Figure 5d), which supports the notion of an enhanced desorption rate for small particles and an equilibrium nanoparticle film size distribution that becomes dominated by large particles.

CONCLUSION

In summary, we have developed DNA-EBL as a method for tuning the local density of active DNA strands in a monolayer by high-resolution, dose-controlled electron-beam irradiation. We have illustrated the potential of DNA-EBL through patterning of nanoparticle monolayer density and size-selective assembly of gold nanoparticles functionalized with complementary DNA. The thermodynamics of polyvalent DNA binding interactions coupled with differences in particle surface area drive this phenomenon. We show that the larger surface coverage by small particles provides a thermodynamic advantage for assembly with high DNA density, but that large particles dominate at low density where small particles cannot access a sufficient number of linkages for immobilization, as supported by molecular dynamics simulations. We anticipate that the technique can be utilized to further the understanding of thermodynamic and kinetic factors in DNA-linked nano-

DOI: 10.1021/acsnano.6b02246
ACS Nano 2016, 10, 5679−5686

particle assembly and to create complex and technologically interesting structures with potential photonic, plasmonic, and bioanalytical applications.

METHODS

DNA Design and Nanoparticle Functionalization. Nanoparticle and substrate functionalization and nanoparticle assembly procedures are similar to previous protocols.[35,40,41] Briefly, oligonucleotides were either synthesized with a MerMade 48 (MM48) automated oligonucleotide synthesizer (BioAutomation) using reagents purchased from Glen Research or purchased (Integrated DNA Technologies). The DNA sequences used are shown in Table 1.

Immediately prior to use, the thiolated oligonucleotides were deprotected by treatment with 100 mM dithiothreitol (DTT) in 170 mM sodium phosphate buffer (pH = 7.4) and purified with Nap-5 size-exclusion columns (GE Healthcare). The purified oligonucleotides were added to gold nanoparticles (British Biocell International) in a ratio of approximately 5 nmol/mL of nanoparticle solution. The solution was placed on a shaker for 2 h to overnight and then brought to 0.01 M sodium phosphate buffer (pH = 7.4) and 0.01 wt % sodium dodecyl sulfate (SDS) in water. Salting buffer (2 M NaCl, 0.01 M sodium phosphate, 0.01 wt % SDS, pH = 7.4) was added stepwise over the course of several hours to bring the final salt concentration to 0.5 M. The nanoparticle solution was placed on shaker overnight and then centrifuged twice and resuspended in 0.01 wt % SDS to remove excess DNA. After a third centrifugation, the nanoparticles were resuspended in storage buffer (0.5 M NaCl, 0.01 M sodium phosphate buffer (pH = 7.4) with 0.01 wt % SDS) at their final concentrations, which were determined by UV−vis. A-type linker strands were added to the nanoparticle suspensions and allowed to fully hybridize by heating the suspension to 60−70 °C and then slowly cooling to room temperature. The linker concentration was 300 per 30 nm nanoparticle and 2000 per 80 nm nanoparticle for most experiments (see Supporting Information for effect of linker concentration).

Substrate Functionalization and Nanoparticle Assembly. Silicon substrates were cleaved, cleaned by oxygen plasma treatment (South Bay Technology, Inc.), and coated with 2 nm of chromium followed by 8 nm of gold in a thermal evaporator (Kurt J. Lesker Company). Following gold coating, substrates were immersed in a substrate buffer (1 M NaCl, 5 mM sodium phosphate buffer (pH = 7.4)), and freshly cleaved and desalted B-Anchor oligonucleotides were added to achieve a DNA concentration of 1 μM. Substrates were placed on a shaker and allowed to react with the thiolated DNA for 24 h followed by rinsing three times in DI water and then were blown dry with nitrogen. After electron-beam exposure, substrates were immersed in storage buffer with 0.5 μM B-type linker oligonucleotides. This solution was heated to 60−70 °C for 30 min and allowed to slowly cool to room temperature to fully hybridize the anchor and linker strands. Substrates were then rinsed three times in storage buffer to remove any unbound DNA.

Nanoparticles were assembled by immersing patterned substrates in the desired nanoparticle mixture, which were placed on a shaker and heated to the desired temperature for a minimum of 5 h. The standard nanoparticle mixture included 2.5 nM small (30 nm) particles and 60 pM large (80 nm) particles for a concentration ratio of 41.7:1. After nanoparticle assembly, substrates were rinsed three times with storage buffer and then embedded in silica[42] to preserve the monolayer structure. For silica embedding, substrates were immersed in 1 mL of storage buffer, 2 μL (7.2 μmol) of *N*-trimethoxysilylpropyl-*N*,*N*,*N*-trimethylammonium chloride (Gelest) was added, and substrates were placed on a shaker for 20 min at 700 rpm. Following this reaction, 4 μL (21.7 μmol) of triethoxysilane (Sigma-Aldrich) was added, and substrates were placed on a shaker for a minimum of 4 h. After silica embedding, each substrate was rinsed three times in DI water and blown dry with nitrogen.

Electron-Beam Modification. Substrates functionalized with B-Anchor oligonucleotides were patterned by electron-beam exposure in a Quanta 600F scanning electron microscope (FEI Company) with an NPGS beam control system (JC Nabity Lithography Systems) and high-speed beam blanker (5 MHz) for pattern generation. All exposures were carried out with a 15 kV accelerating voltage and 6.5 mm working distance. High-resolution patterns were exposed using a small spot size, low beam current (~200 pA) and small pixel spacing (~3 nm). Large-area patterns were exposed with a large beam current (~8 nA) and larger pixel spacing (~100 nm). Since the beam size may be smaller than the pixel size under the latter conditions, the beam was defocused 25 μm. This defocus was determined empirically to be sufficient to minimize pixel-size artifacts in subsequent nanoparticle assembly.

X-ray Photoelectron Spectroscopy. XPS analysis was carried out with an ESCALAB 250Xi (Thermo Scientific). Large 1 mm^2 regions on B-Anchor DNA functionalized silicon substrates were exposed to ensure no overlap of the 500 μm X-ray probe with unexposed regions. C 1s scans were carried out by averaging 100 scans with a pass energy of 20 eV, dwell time of 100 ms, and energy step size of 0.1 eV with electron-beam flood for charge suppression. While charging was minimal, an energy shift was applied according to Au 4f reference scans for each sample. A Gaussian/Lorentzian mixed peak fit was carried out for the four characteristic peaks near 284.5, 286, 287.5, and 289 eV.

Fluorescence Microscopy. Fluorescence microscopy was carried out with an IX83 inverted fluorescent microscope (Olympus) using a Cy5 filter. Semiquantitative analysis was performed by calculating relative intensity values for the modified regions compared to an immediately adjacent unmodified region. This method minimized the effects of uneven illumination and any long-range variations or gradients in DNA loading on the substrate.

Scanning Electron Microscopy (SEM). SEM analysis was performed with a SU8030 cold-cathode, field-emission SEM (Hitachi) with 5 kV accelerating voltage and upper backscattered electron detector to minimize contrast from the silica sol−gel. Image analysis was performed with a custom MatLab script described in the Supporting Information.

Molecular Dynamics Simulation. Coarse-grained canonical molecular dynamics simulations were performed of the surface adsorption behavior of solutions with a bimodal distribution of particles, including 88 small (30 nm) and 8 large (80 nm) nanoparticles, grafted with bead−spring chains, at varying surface modification levels. The simulations are described in detail in the Supporting Information.

ASSOCIATED CONTENT

Supporting Information

The Supporting Information is available free of charge on the ACS Publications website at DOI: 10.1021/acsnano.6b02246.

Spectrophotometry, effects of nanoparticle and linker concentration, image processing, surface coverage calculations, MD simulation details (PDF)
SI Video 1: MD simulation movie (AVI)
SI Video 2: MD simulation movie (AVI)

AUTHOR INFORMATION

Corresponding Author

*E-mail: v-dravid@northwestern.edu.

Notes

The authors declare no competing financial interest.

ACKNOWLEDGMENTS

The authors thank C. Ramavarapu for assistance with computer simulations and D. Myers for valuable discussions. The SEM, EBL, and XPS work made use of the EPIC and Keck-II facilities in the NUANCE Center at Northwestern University which has received support from the MRSEC program (NSF DMR-1121262) at the Materials Research Center; the Soft and Hybrid Nanotechnology Experimental (SHyNE) Resource

DOI: 10.1021/acsnano.6b02246
ACS Nano 2016, 10, 5679−5686

(NSF NNCI-1542205); and the International Institute for Nanotechnology (IIN); the Keck Foundation and the State of Illinois, through the IIN. Fluorescence microscopy was performed at the Northwestern University Quantitative Bioelement Imaging Center. The experimental work was supported by the Air Force Office of Scientific Research under Award No. FA9550-12-1-0280. Q.-Y.L. gratefully acknowledges support through a Ryan Fellowship at Northwestern University. The computer simulations were supported by the National Science Foundation through Grants DMR-1121262 and DMR-1310211.

REFERENCES

(1) Shevchenko, E. V.; Talapin, D. V.; Kotov, N. A.; O'Brien, S.; Murray, C. B. Structural Diversity in Binary Nanoparticle Superlattices. *Nature* **2006**, *439*, 55−59.
(2) Park, S. Y.; Lytton-Jean, A. K. R.; Lee, B.; Weigand, S.; Schatz, G. C.; Mirkin, C. A. DNA-Programmable Nanoparticle Crystallization. *Nature* **2008**, *451*, 553−556.
(3) Nykypanchuk, D.; Maye, M. M.; van der Lelie, D.; Gang, O. DNA-Guided Crystallization of Colloidal Nanoparticles. *Nature* **2008**, *451*, 549−552.
(4) Kuzyk, A.; Schreiber, R.; Fan, Z.; Pardatscher, G.; Roller, E.-M.; Högele, A.; Simmel, F. C.; Govorov, A. O.; Liedl, T. DNA-Based Self-Assembly of Chiral Plasmonic Nanostructures with Tailored Optical Response. *Nature* **2012**, *483*, 311−314.
(5) Tan, S. J.; Campolongo, M. J.; Luo, D.; Cheng, W. Building Plasmonic Nanostructures with DNA. *Nat. Nanotechnol.* **2011**, *6*, 268−276.
(6) Park, D. J.; Zhang, C.; Ku, J. C.; Zhou, Y.; Schatz, G. C.; Mirkin, C. A. Plasmonic Photonic Crystals Realized through DNA-Programmable Assembly. *Proc. Natl. Acad. Sci. U. S. A.* **2015**, *112*, 977−981.
(7) Anker, J. N.; Hall, W. P.; Lyandres, O.; Shah, N. C.; Zhao, J.; Van Duyne, R. P. Biosensing with Plasmonic Nanosensors. *Nat. Mater.* **2008**, *7*, 442−453.
(8) Park, S.-J.; Taton, T. A.; Mirkin, C. A. Array-Based Electrical Detection of DNA with Nanoparticle Probes. *Science* **2002**, *295*, 1503−1506.
(9) Agrios, A. G.; Cesar, I.; Comte, P.; Nazeeruddin, M.; Grätzel, M. Nanostructured Composite Films for Dye-Sensitized Solar Cells by Electrostatic Layer-by-Layer Deposition. *Chem. Mater.* **2006**, *18*, 5395−5397.
(10) Zijlstra, P.; Chon, J. W.; Gu, M. Five-Dimensional Optical Recording Mediated by Surface Plasmons in Gold Nanorods. *Nature* **2009**, *459*, 410−413.
(11) Cargnello, M.; Johnston-Peck, A. C.; Diroll, B. T.; Wong, E.; Datta, B.; Damodhar, D.; Doan-Nguyen, V. V. T.; Herzing, A. A.; Kagan, C. R.; Murray, C. B. Substitutional Doping in Nanocrystal Superlattices. *Nature* **2015**, *524*, 450−453.
(12) Boles, M. A.; Talapin, D. V. Many-Body Effects in Nanocrystal Superlattices: Departure from Sphere Packing Explains Stability of Binary Phases. *J. Am. Chem. Soc.* **2015**, *137*, 4494−4502.
(13) Nie, Z.; Petukhova, A.; Kumacheva, E. Properties and Emerging Applications of Self-Assembled Structures Made from Inorganic Nanoparticles. *Nat. Nanotechnol.* **2010**, *5*, 15−25.
(14) Mirkin, C. A.; Letsinger, R. L.; Mucic, R. C.; Storhoff, J. J. A DNA-Based Method for Rationally Assembling Nanoparticles into Macroscopic Materials. *Nature* **1996**, *382*, 607−609.
(15) Jones, M. R.; Seeman, N. C.; Mirkin, C. A. Programmable Materials and the Nature of the DNA Bond. *Science* **2015**, *347*, 1260901.
(16) Macfarlane, R. J.; Lee, B.; Jones, M. R.; Harris, N.; Schatz, G. C.; Mirkin, C. A. Nanoparticle Superlattice Engineering with DNA. *Science* **2011**, *334*, 204−208.
(17) Auyeung, E.; Li, T. I. N. G.; Senesi, A. J.; Schmucker, A. L.; Pals, B. C.; de la Cruz, M. O.; Mirkin, C. A. DNA-Mediated Nanoparticle Crystallization into Wulff Polyhedra. *Nature* **2014**, *505*, 73−77.
(18) Senesi, A. J.; Eichelsdoerfer, D. J.; Macfarlane, R. J.; Jones, M. R.; Auyeung, E.; Lee, B.; Mirkin, C. A. Stepwise Evolution of DNA-Programmable Nanoparticle Superlattices. *Angew. Chem., Int. Ed.* **2013**, *52*, 6624−6628.
(19) Ku, J. C.; Ross, M. B.; Schatz, G. C.; Mirkin, C. A. Conformal, Macroscopic Crystalline Nanoparticle Sheets Assembled with DNA. *Adv. Mater.* **2015**, *27*, 3159−3163.
(20) Taton, T. A.; Mirkin, C. A.; Letsinger, R. L. Scanometric DNA Array Detection with Nanoparticle Probes. *Science* **2000**, *289*, 1757−1760.
(21) Lin, Q.-Y.; Li, Z.; Brown, K. A.; O'Brien, M. N.; Ross, M. B.; Zhou, Y.; Butun, S.; Chen, P.-C.; Schatz, G. C.; Dravid, V. P. Strong Coupling between Plasmonic Gap Modes and Photonic Lattice Modes in DNA-Assembled Gold Nanocube Arrays. *Nano Lett.* **2015**, *15*, 4699−4703.
(22) Roller, E.-M.; Khorashad, L. K.; Fedoruk, M.; Schreiber, R.; Govorov, A. O.; Liedl, T. DNA-Assembled Nanoparticle Rings Exhibit Electric and Magnetic Resonances at Visible Frequencies. *Nano Lett.* **2015**, *15*, 1368−1373.
(23) Ross, M. B.; Mirkin, C. A.; Schatz, G. C. Optical Properties of One-, Two-, and Three-Dimensional Arrays of Plasmonic Nanostructures. *J. Phys. Chem. C* **2016**, *120*, 816−830.
(24) Storhoff, J. J.; Lazarides, A. A.; Mucic, R. C.; Mirkin, C. A.; Letsinger, R. L.; Schatz, G. C. What Controls the Optical Properties of DNA-Linked Gold Nanoparticle Assemblies? *J. Am. Chem. Soc.* **2000**, *122*, 4640−4650.
(25) Hurst, S. J.; Hill, H. D.; Mirkin, C. A. Three-Dimensional Hybridization" with Polyvalent DNA− Gold Nanoparticle Conjugates. *J. Am. Chem. Soc.* **2008**, *130*, 12192−12200.
(26) Macfarlane, R. J.; Thaner, R. V.; Brown, K. A.; Zhang, J.; Lee, B.; Nguyen, S. T.; Mirkin, C. A. Importance of the DNA "Bond" in Programmable Nanoparticle Crystallization. *Proc. Natl. Acad. Sci. U. S. A.* **2014**, *111*, 14995−15000.
(27) Myers, B. D.; Dravid, V. P. Variable Pressure Electron Beam Lithography (VP-*e*BL): A New Tool for Direct Patterning of Nanometer-Scale Features on Substrates with Low Electrical Conductivity. *Nano Lett.* **2006**, *6*, 963−968.
(28) Donthu, S.; Pan, Z.; Myers, B.; Shekhawat, G.; Wu, N.; Dravid, V. Facile Scheme for Fabricating Solid-State Nanostructures Using E-Beam Lithography and Solution Precursors. *Nano Lett.* **2005**, *5*, 1710−1715.
(29) Isaacson, M.; Johnson, D.; Crewe, A. V. Electron Beam Excitation and Damage of Biological Molecules; Its Implications for Specimen Damage in Electron Microscopy. *Radiat. Res.* **1973**, *55*, 205−224.
(30) Lett, J.; Alexander, P. Crosslinking and Degradation of Deoxyribonucleic Acid Gels with Varying Water Contents When Irradiated with Electrons. *Radiat. Res.* **1961**, *15*, 159−173.
(31) Tiberio, R.; Craighead, H.; Lercel, M.; Lau, T.; Sheen, C.; Allara, D. Self-Assembled Monolayer Electron Beam Resist on GaAs. *Appl. Phys. Lett.* **1993**, *62*, 476−478.
(32) Zhang, G.-J.; Tanii, T.; Funatsu, T.; Ohdomari, I. Patterning of DNA Nanostructures on Silicon Surface by Electron Beam Lithography of Self-Assembled Monolayer. *Chem. Commun.* **2004**, 786−787.
(33) Jin, R.; Wu, G.; Li, Z.; Mirkin, C. A.; Schatz, G. C. What Controls the Melting Properties of DNA-Linked Gold Nanoparticle Assemblies? *J. Am. Chem. Soc.* **2003**, *125*, 1643−1654.
(34) Demers, L. M.; Mirkin, C. A.; Mucic, R. C.; Reynolds, R. A.; Letsinger, R. L.; Elghanian, R.; Viswanadham, G. A Fluorescence-Based Method for Determining the Surface Coverage and Hybridization Efficiency of Thiol-Capped Oligonucleotides Bound to Gold Thin Films and Nanoparticles. *Anal. Chem.* **2000**, *72*, 5535−5541.
(35) O'Brien, M. N.; Radha, B.; Brown, K. A.; Jones, M. R.; Mirkin, C. A. Langmuir Analysis of Nanoparticle Polyvalency in DNA-Mediated Adsorption. *Angew. Chem., Int. Ed.* **2014**, *53*, 9532−9538.
(36) May, C. J.; Canavan, H. E.; Castner, D. G. Quantitative X-Ray Photoelectron Spectroscopy and Time-of-Flight Secondary Ion Mass

DOI: 10.1021/acsnano.6b02246
ACS Nano 2016, 10, 5679−5686

Spectrometry Characterization of the Components in DNA. *Anal. Chem.* **2004**, *76*, 1114−1122.
(37) Ptasińska, S.; Stypczynska, A.; Nixon, T.; Mason, N.; Klyachko, D. V.; Sanche, L. X-Ray Induced Damage in DNA Monitored by X-Ray Photoelectron Spectroscopy. *J. Chem. Phys.* **2008**, *129*, 065102.
(38) Hill, H. D.; Millstone, J. E.; Banholzer, M. J.; Mirkin, C. A. The Role Radius of Curvature Plays in Thiolated Oligonucleotide Loading on Gold Nanoparticles. *ACS Nano* **2009**, *3*, 418−424.
(39) Lee, J.-S.; Stoeva, S. I.; Mirkin, C. A. DNA-Induced Size-Selective Separation of Mixtures of Gold Nanoparticles. *J. Am. Chem. Soc.* **2006**, *128*, 8899−8903.
(40) Hill, H. D.; Mirkin, C. A. The Bio-Barcode Assay for the Detection of Protein and Nucleic Acid Targets Using DTT-Induced Ligand Exchange. *Nat. Protoc.* **2006**, *1*, 324−336.
(41) Senesi, A. J.; Eichelsdoerfer, D. J.; Brown, K. A.; Lee, B.; Auyeung, E.; Choi, C. H. J.; Macfarlane, R. J.; Young, K. L.; Mirkin, C. A. Oligonucleotide Flexibility Dictates Crystal Quality in DNA-Programmable Nanoparticle Superlattices. *Adv. Mater.* **2014**, *26*, 7235−7240.
(42) Auyeung, E.; Macfarlane, R. J.; Choi, C. H. J.; Cutler, J. I.; Mirkin, C. A. Transitioning DNA-Engineered Nanoparticle Superlattices from Solution to the Solid State. *Adv. Mater.* **2012**, *24*, 5181−5186.

DOI: 10.1021/acsnano.6b02246
ACS Nano 2016, 10, 5679−5686